Materials Advances

ROYAL SOCIETY OF CHEMISTRY

PAPER

View Article Online
View Journal | View Issue

Cite this: *Mater. Adv.*, 2025, 6, 2530

High-concentration Mn^{4+} doping in boron-modified $Ca_{14}Zn_6Al_{10}O_{35}$ – based phosphors: decoding superior luminescence performances†

Jiquan Huang, *[ab] Ting Lv,[a] Yuqing Lin,[a] Zhonghua Deng,[a] Zhuguang Liu[a] and Wang Guo *[ab]

Received 23rd January 2025,
Accepted 19th February 2025

DOI: 10.1039/d5ma00059a

rsc.li/materials-advances

The application prospects of Mn^{4+}-activated oxide phosphors are hindered by their relatively weak absorption of blue light, which stems mainly from severe concentration quenching. $Ca_{14}Zn_6Al_{10}O_{35}:Mn^{4+}$, noted for its high quantum efficiency and minimal thermal quenching, experiences concentration quenching arising from the direct energy transfer from Mn^{4+} ions to the adjacent crystal defects. In this study, a synergistic strategy involving B_2O_3 flux and B^{3+} doping was introduced to mitigate the crystal defects. This strategy elevates the optimal Mn^{4+} doping concentration effectively from 1% to 6%, thereby ensuring efficient light absorption in the UV-to-blue band and facilitating intense deep-red emission within the 650–780 nm range. Notably, the quantum efficiency remains above 90% with Mn^{4+} doping levels ranging from 1% to 5%. The emission intensity remains stable between 300 and 460 K, with a marked decline only above 500 K. Additionally, the decay lifetime exhibits a linear variation with temperature. These characteristics suggest that the optimal phosphors hold great promise for applications in areas such as indoor agriculture, luminescent thermometers, and solar cells.

1. Introduction

With the widespread application of solid-state lighting based on phosphor-converted light-emitting diodes (LEDs) for general lighting, indoor agriculture, and liquid crystal display backlighting, there is a high demand for efficient red-emitting phosphors excited by InGaN-based LED chips (λ = 360–470 nm).[1–3] The most popular commercial white LED lamps are fabricated by merging broadband-emitting yellow and red phosphors on a blue LED chip, or alternatively, by coating red, green and blue phosphors on a near-ultraviolet (NUV) LED chip.[4–6] In the context of agriculture lighting, an LED lamp capable of promoting plant growth should emit blue (420–500 nm) and red (640–750 nm) light, as photons with these wavelengths are indispensable for the four main plant pigments (chlorophyll *a* and *b*, phytochrome P_R and P_{FR}).[7,8] When LEDs are used as backlight, narrowband-emitting red phosphors are essential.[9,10] In addition, red-emitting phosphors can serve as spectral converters in photovoltaic devices to enhance conversion efficiency, since they can convert incident high-energy phonons (typically, with $\lambda < 520$ nm) that cannot be utilized efficiently by the photovoltaic materials into long wavelength photons (with λ = 630–750 nm) to which the solar cells have a better response.[11–13]

The current commercial red-emitting phosphors fall mainly into two categories: Eu^{2+}-activated nitrides and Mn^{4+}-activated fluorides. The former, such as $Sr_2Si_5N_8:Eu^{2+}$ and $CaAlSiN_3:Eu^{2+}$, excel in blue LED absorption, quantum efficiency (QE), and chemical stability.[14–16] However, they exhibit serious reabsorption of green/yellow light emitted by other phosphors, which leads to color offset and diminished luminous efficacy of LED devices.[16,17] In comparison, Mn^{4+}-doped fluorides (and oxyfluorides), represented by $K_2SiF_6:Mn^{4+}$, offer narrow-band red emission between 610 and 650 nm, and efficient blue light excitation at approximately 460 nm with absorption cut-off around 510 nm.[18] Nevertheless, they suffer from poor chemical/thermal stability and environmental hazards.[19,20] The inherent drawbacks of nitrides and fluorides have thus spurred the search for alternative materials. Mn^{4+}-activated oxides, with their innate advantages such as environmental friendliness, cost-efficiency, narrow-band deep-red emission, and especially outstanding thermal and chemical stability, have drawn escalating attention.[19–21]

The excitation spectrum of Mn^{4+}-activated phosphors typically features broad absorption bands in the NUV-to-xvisible wavelength range, arising mainly from the spin-allowed

[a] *Key Laboratory of Optoelectronic Materials Chemistry and Physics, Fujian Institute of Research on the Structure of Matter, Chinese Academy of Sciences, Fuzhou 350002, P. R. China. E-mail: hjq@fjirsm.ac.cn, guowang@fjirsm.ac.cn*
[b] *Fujian Science & Technology Innovation Laboratory for Optoelectronic Information of China, Fuzhou 350108, P. R. China*

† Electronic supplementary information (ESI) available. See DOI: https://doi.org/10.1039/d5ma00059a

$^4A_{2g} \rightarrow {}^4T_{2g}$, $^4A_{2g} \rightarrow {}^4T_{1g,a}(^4F)$, and $^4A_{2g} \rightarrow {}^4T_{1g,b}(^4P)$ transitions within the 3d orbitals of the Mn^{4+} ions.[3,21] However, these transitions are parity-forbidden since they occur between levels of the d shell.[22,23] As a result, the molar absorption coefficient for Mn^{4+} is indeed low compared to that for Ce^{3+} or Eu^{2+}. This challenge is more pronounced in oxide materials, since the optimal Mn^{4+} doping concentration is approximately 5% for fluorides but falls below 1% for most oxides. Therefore, a high Mn^{4+} doping concentration (*e.g.*, 5%) in oxides is crucial for ensuring sufficient absorption of blue light, as it holds great significance for their prospective commercial viability.[24] Notably, as the doping concentration of Mn^{4+} increases, the emission intensity and QE will decline once effective concentration quenching takes place. This is an issue that warrants particular attention.

According to Dexter's theory,[25,26] concentration quenching in inorganic phosphors occurs as a result of the migration of excitation energy from one activator center to another until it reaches an imperfection that serves as an energy sink. His research reveals that, for activators with electric dipole or electric quadrupole transitions, quenching phenomena are likely to emerge when the activator concentration is on the order of 10^{-3} to 10^{-2}. As previously indicated, such a concentration level is considerably insufficient for Mn^{4+} ions to achieve optimal performance. However, this is exactly the circumstance observed in the majority of Mn^{4+}-activated oxides. The concentration quenching in Mn^{4+}-activated oxides is principally attributed to the multi-polar interaction.[24,27–29] Recently, we performed a study on the fundamental luminescence properties of Mn^{4+}-activated $Ca_{14}Zn_6Al_{10}O_{35}$ (CZAO:Mn^{4+}).[30] It was found that the concentration quenching in this compound arises mainly from the direct energy transfer from Mn^{4+} ions to neighboring defects, which is consistent with the observations in fluorides possessing high Mn^{4+} doping concentrations such as K_2SiF_6:Mn^{4+} and $RbSbF_6$:Mn^{4+}.[31,32] This finding implies that high-concentration doping and high QE can be achieved by reducing crystal defects in CZAO:Mn^{4+} phosphors. The primary crystal defects in CZAO:Mn^{4+} phosphors are oxygen vacancies and zinc vacancies, as well as Mn^{5+} or Mn^{2+} ions, which are generated during the high-temperature sintering process.[30,33]

In this study, we propose to introduce B_2O_3 as a flux to lower the sintering temperature, improve the crystallinity, and inhibit the volatilization of Zn, thereby reducing the crystal defects and mitigating the concentration quenching. The experiment results show that, in the high-temperature solid-state reaction, B_2O_3 not only functions as a flux, but also enables some B^{3+} ions to occupy the lattice sites of CZAO host. This synergistic effect improves the optimal Mn^{4+} doping concentration in CZAO from 1% to 6%, ensuring sufficient light absorption in the NUV-to-blue band. The optimized $Ca_{14}Zn_6Al_{9.85-2x}B_{0.15}Mn_xMg_xO_{35}$ − 0.42% B_2O_3 phosphors exhibit high QE exceeding 90% when the doping concentrations of Mn^{4+} are between 1% and 5%, which is much higher than the 76.8% for $Ca_{14}Zn_6Al_{9.8}Mn_{0.1}Mg_{0.1}O_{35}$ without B-modification. Based on the experimental results, we conducted a thorough analysis of the photoluminescence performances of B-modified CZAO:Mn^{4+} phosphors, and evaluated their potential applications in indoor agricultural lighting, optical thermometers, and solar cells.

2. Experimental section

2.1. Sample preparation

Three groups of phosphors, namely $Ca_{14}Zn_6Al_{9.8}Mn_{0.1}Mg_{0.1}O_{35}$ − *z* wt% B_2O_3, $Ca_{14}Zn_6Al_{9.8-y}B_yMn_{0.1}Mg_{0.1}O_{35}$, and $Ca_{14}Zn_6Al_{9.85-2x}B_{0.15}Mn_xMg_xO_{35}$ − 0.42% B_2O_3, were synthesized by the traditional solid-state reaction method. $CaCO_3$ (99.9%), ZnO (99.9%), Al_2O_3 (99.9%), $MnCO_3$ (99.95%), MgO (99.9%), and H_3BO_3 (99.5%) were employed as the starting materials (note: H_3BO_3 will dehydrate during calcination, and we assume that the solid product is exclusively B_2O_3. Hence, the chemical composition of the sample is labeled as B_2O_3 instead of H_3BO_3. Correspondingly, the dosage of H_3BO_3 is weighed according to the stoichiometric ratio of B_2O_3). These reagents were mixed in stoichiometric proportions and ball-milled in ethanol for 24 h. The resulting slurry was dried, ground, and sieved. The obtained fine powders were calcined in a muffle furnace at 1220–1280 °C under an oxygen-rich atmosphere to obtain the final products.

2.2. Characterizations

The crystal structure of the obtained phosphors was analyzed by powder X-ray diffraction (XRD, Mini Flex600, Rigaku, Japan) with Cu Kα radiation. The reflection was measured by an UV-Vis-NIR spectrophotometer (Lambda-900, PerkinElmer, USA). The photoluminescence excitation (PLE) and emission (PL) spectra, and PL decays of the samples were measured with an FLS1000 luminescence spectrometer (British Edinburgh Instrument Company) equipped with red photomultiplier tube (R928P; spectral range: 200–870 nm) as detector. For temperature-dependent measurement from 80 to 660 K, the samples were placed on a thermal stage (HFS 600, Linkam Scientific Instruments). For QE measurement, the sample was put inside an optical integrating sphere coupled to the spectrometer. For evaluating the electroluminescence (EL) performance, LEDs were fabricated by integrating the phosphors on a blue InGaN LED chip (λ = 450 nm) mounting on a metal-backed printed circuit board, and their optical properties were tested by using the integrated optical and electrical measuring system (Everfine, Hangzhou).

3. Results and discussion

3.1. Effect of B_2O_3 flux on crystallinity and photoluminescence

Fig. 1a shows the XRD patterns of $Ca_{14}Zn_6Al_{9.8}Mn_{0.1}Mg_{0.1}O_{35}$ phosphors sintered at different temperatures for 5 h, which indicates that the optimal sintering temperature is approximately 1250 °C. Variation in sintering temperature, both higher and lower, can be detrimental to phase purity. For instance, when sintered at 1220 °C, the sample contained unreacted CaO, ZnO, and the intermediate product $Ca_{12}Al_{14}O_{33}$. Even when the temperature was increased to 1240 °C, a trace of $Ca_{12}Al_{14}O_{33}$ was still detected. In principle, raising the sintering temperature promotes the solid-state reactions and enhances the crystallinity of the final product, but it also intensifies the volatilization of zinc.[33] When the sintering temperature was raised to 1280 °C, the significant volatilization of zinc led to

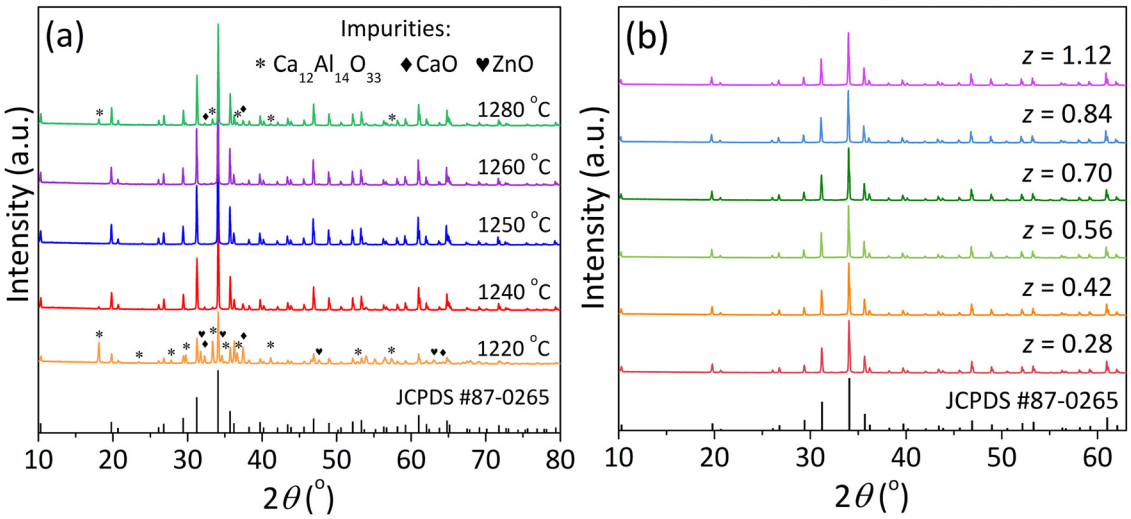

Fig. 1 XRD patterns of (a) $Ca_{14}Zn_6Al_{9.8}Mn_{0.1}Mg_{0.1}O_{35}$ phosphors sintered at various temperatures for 5 h, and (b) $Ca_{14}Zn_6Al_{9.8}Mn_{0.1}Mg_{0.1}O_{35}$ – z wt% B_2O_3 phosphors sintered at 1240 °C for 4 h. The standard diffraction pattern of $Ca_{14}Zn_6Al_{10}O_{35}$ from JCPDS (No. 87-0265) is provided at the bottom of the figure.

partial decomposition of CZAO, subsequently regenerating impurities including $Ca_{12}Al_{14}O_{33}$ and CaO. Fig. 1b shows the XRD patterns of the $Ca_{14}Zn_6Al_{9.8}Mn_{0.1}Mg_{0.1}O_{35}$ phosphors with different amounts of B_2O_3 flux, which were sintered at 1240 °C for 4 h, and no diffraction peak of impurity phase was observed. This indicates that the introduction of B_2O_3 flux can reduce the sintering temperature and time, which is of great significance in preventing crystal defects caused by zinc volatilization.

The B_2O_3 flux not only promotes the crystallization of CZAO but also enhances its photoluminescence properties. Fig. 2a shows the PLE spectra of $Ca_{14}Zn_6Al_{9.8}Mn_{0.1}Mg_{0.1}O_{35}$ – z wt% B_2O_3 phosphors, which indicate strong absorption from UV (~250 nm) to visible light region (~530 nm). The PLE spectrum can be decomposed into five Gaussian peaks located at approximately 464, 397, 332, 289, and 258 nm. These peaks correspond to the transitions from the ground state ($^4A_{2g}$) to the $^4T_{2g}$, $^2T_{2g}$, $^4T_{1g,a}$, $^2A_{1g}$, and $^4T_{1g,b}$ (or charge transfer (CT) band) excitation states, respectively.[30] Fig. 2c shows the PL spectra of the samples, featuring five sharp peaks at about 677, 686, 695, 705, and 713 nm. These peaks can be attributed to the anti-Stokes ν_4 and ν_6 vibrations, the zero-phonon line (ZPL), and the Stokes ν_6 and ν_4 vibrations, respectively.[33,34] With the increase in B_2O_3 content, the PLE and PL intensities initially increased and then decreased. As shown in panels (b) and (d) of Fig. 2, when the B_2O_3 content reached 0.42 wt% (z = 0.42), both the PLE and PL intensities reached their maximum, increasing by 87% and 112%, respectively, compared to the sample without B_2O_3 (z = 0). The QE also showed an improvement, increasing from 76.8% at z = 0 to 84.6% at z = 0.42, and remaining above 83% when $0.28 \leq z \leq 0.56$. The improvement in light absorption/emission, as well as the QE, can be attributed primarily to the improved crystallinity and the reduced crystal defects facilitated by the B_2O_3 flux. Besides, the introduction of B_2O_3 was found to alter the profile of the PLE spectrum. As shown in Fig. 2b, the percentage of the $^4A_{2g} \rightarrow {}^4T_{2g}$ transition in the PLE spectrum increased rapidly from 25% at z = 0 to 35% at z = 0.28, and then leveled off at around 36% with further increases in B_2O_3 content. This observation suggests that some B atoms may occupy the lattice site of CZAO. To verify this hypothesis, we prepared B-doped CZAO samples and studied their spectral properties, as detailed below.

3.2. Effect of B^{3+}-doping on crystallinity and photoluminescence

Fig. 3 shows the XRD patterns of the $Ca_{14}Zn_6Al_{9.8-y}B_y$-$Mn_{0.1}Mg_{0.1}O_{35}$ phosphors. As the B^{3+} doping concentration increased, the diffraction peaks shifted slightly towards higher angles when $y \leq 0.2$, and remained almost unchanged for $y >$ 0.2. This shift is attributed to the substitution of Al^{3+} ions by the smaller B^{3+} ions, which reduces the lattice parameters. These results indicate that B^{3+} ions were successfully incorporated into the CZAO lattice, with a solid solubility limit of about 2% (y = 0.2). Beyond this threshold, excessive B^{3+} ions cannot enter the crystal lattice, which will lead to the formation of Al vacancies. Meanwhile, the volatilization of Zn will result in Zn vacancies.[33] The scarcity of cations in the Al and Zn sites creates crystal defects and potentially gives rise to impurity phases. Notably, at y = 0.7, CaO minor phase was detected in the sample, which can be attributed to the relative excess of Ca compared to the deficiency of Al and Zn.

Fig. 4 shows the reflectance spectra of the $Ca_{14}Zn_6Al_{9.8-y}$-$B_yMn_{0.1}Mg_{0.1}O_{35}$ ($0 \leq y \leq 0.70$) phosphors. There were four remarkable absorption peaks located at about 460, 350, 260, and 225 nm, corresponding to the $^4A_{2g} \rightarrow {}^4T_{2g}$, $^4A_{2g} \rightarrow {}^4T_{1g,a}$, $^4A_{2g} \rightarrow {}^4T_{1g,b}$ (and/or CT band) transitions, and host lattice absorption, respectively.[21,33] Noticeably, the absorption of blue light around 460 nm (as well as UV light around 360 nm) was enhanced continuously with increasing B^{3+} doping concentration, reaching the maximum at y = 0.20, and then began to decrease with further increases in B content. This occurrence is highly associated with the doping behavior of B^{3+} in the CZAO lattice. As shown in Fig. 3, the doping limit of B^{3+} in CZAO is about 2%, and the corresponding sample exhibits the most

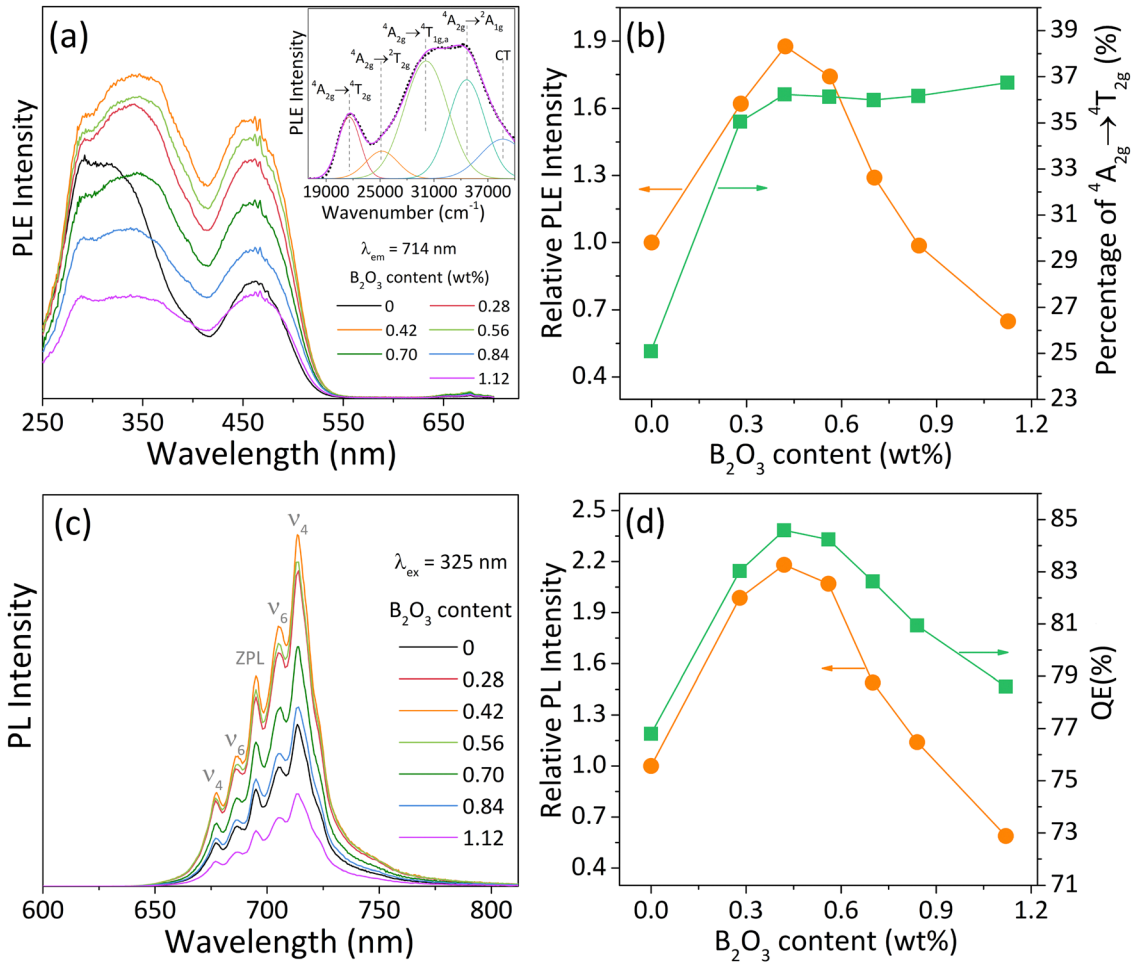

Fig. 2 (a) Room-temperature PLE spectra of $Ca_{14}Zn_6Al_{9.8}Mn_{0.1}Mg_{0.1}O_{35}$ – z wt% B_2O_3 phosphors. The inset shows the deconvoluted PLE spectrum of $Ca_{14}Zn_6Al_{9.8}Mn_{0.1}Mg_{0.1}O_{35}$ without B_2O_3 additive using Gaussian fitting. (b) Dependence of the PLE intensity and the percentage of $^4A_{2g} \rightarrow {}^4T_{2g}$ transition (*i.e.*, blue light absorption) in the ~250–550 nm spectral region on the weight content of B_2O_3. (c) Room-temperature PL spectra of $Ca_{14}Zn_6Al_{9.8}Mn_{0.1}Mg_{0.1}O_{35}$ – z wt% B_2O_3 phosphors. (d) Dependence of the PL intensity and QE on the weight content of B_2O_3.

powerful blue light absorption ability. However, further increase in boron content promotes the generation of crystal defects and may even induce the formation of impurities (such as CaO), which in turn leads to a decrease in the light absorption capacity.

Fig. 5a presents the PL spectra of the $Ca_{14}Zn_6Al_{9.8-y}B_yMn_{0.1}Mg_{0.1}O_{35}$ phosphors, revealing a strong dependence of luminescence intensity on the B^{3+} doping level, with a similar pattern to that of light absorption. Fig. 5b illustrates that the emission intensity surged with increasing boron content, peaking at $y = 0.15$, where it was 1.9 times that of the undoped case ($y = 0$). Subsequently, the emission intensity began to decline, dropping to 83% of the undoped level at $y = 0.7$. Concurrently, the QE increased from 76.8% at $y = 0$ to 84.7% at $y = 0.15$, then decreases progressively to 83.2% at $y = 0.7$.

3.3. Photoluminescence properties of $Ca_{14}Zn_6Al_{9.85-2x}B_{0.15}Mn_xMg_xO_{35}$ – 0.42% B_2O_3 phosphors

It is found from the above experimental results that the ideal amount of B_2O_3 flux is about 0.42%, and the optimal doping concentration of B^{3+} ions in the CZAO lattice is approximately 1.5% ($y = 0.15$). Therefore, we synthesized a series of $Ca_{14}Zn_6Al_{9.85-2x}B_{0.15}Mn_xMg_xO_{35}$ phosphors with the addition of 0.42% B_2O_3 flux to investigate their photoluminescence performance. Particularly focusing on the concentration quenching and thermal quenching.

Fig. 6a presents the PLE spectra of the $Ca_{14}Zn_6Al_{9.85-2xx}B_{0.15}Mn_xMg_xO_{35}$ – 0.42% B_2O_3 samples. With the increase in Mn^{4+} content (x), the excitation peak broadened and its intensity increased. This led to the gradual disappearance of the valley positioned at around 415 nm, which was discernible in the sample with $x = 0.1$ and those without B-modification (see Fig. 2a). Concomitantly, the full width at half maximum (FWHM) expanded progressively from 240 nm when $x = 0.1$ to 280 nm when $x = 0.6$. The pronounced light absorption within the 360–500 nm range for samples with $x > 0.2$ endows them highly compatible with the current mainstream NUV and blue LED chips. The PLE intensity reached a maximum at $x = 0.6$ and declined subsequently, indicating that concentration quenching becomes significant. The PL spectra of the samples are presented in Fig. 6b, and the dependence of PL intensity on

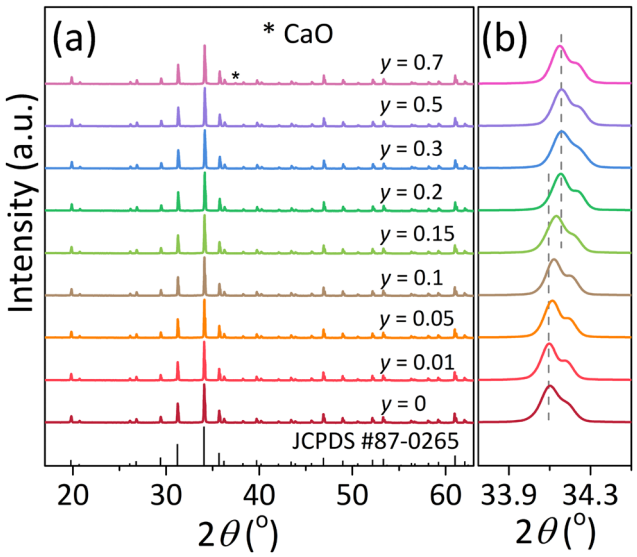

Fig. 3 (a) XRD patterns of the $Ca_{14}Zn_6Al_{9.8-y}B_yMn_{0.1}Mg_{0.1}O_{35}$ phosphors sintered at 1250 °C for 5 h, (b) enlarged patterns around 2θ = 34.1°.

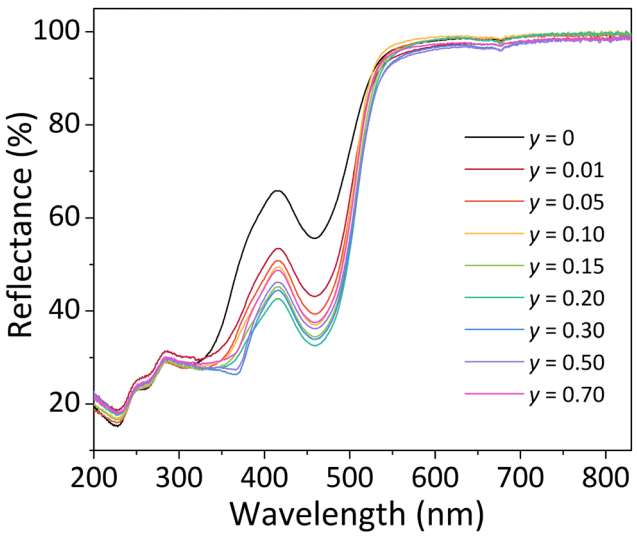

Fig. 4 Reflectance spectra of the $Ca_{14}Zn_6Al_{9.8-y}B_yMn_{0.1}Mg_{0.1}O_{35}$ phosphors.

Mn^{4+} doping concentration is illustrated in Fig. 6c. Similar to the PLE spectra, the emission intensity reached its maximum at x = 0.6. Therefore, it can be considered that the critical concentration of Mn^{4+} in $Ca_{14}Zn_6Al_{9.85-2x}B_{0.15}Mn_xMg_xO_{35}$ − 0.42% B_2O_3 is 6% (x = 0.6). Correspondingly, the critical distance (R_c) was calculated to be approximately 19 Å, which means that energy migration through short-range exchange interactions among Mn^{4+} ions is infeasible.[24,30,32] In fact, for the reported Mn^{4+}-activated oxides that we know of, Mn^{4+} ions cannot form neighbors within 5 Å due to their low doping concentration. Alternatively, concentration quenching of Mn^{4+} ions in oxide hosts is usually attributed to the multi-polar interactions, which can be described by the following equation based on Dexter theory:[24,29,35]

$$\frac{I}{x} = \frac{K}{1+\beta x^{\theta/3}} \quad (1)$$

which is equivalent to

$$\frac{x}{I} = \frac{1}{K} + \frac{\beta}{K}x^{\theta/3} \quad (2)$$

where I represents the integrated PL intensity, K and β are constants for a given host lattice, and θ is an indicative factor of the interaction with θ = 6, 8, and 10 corresponding to the dipole–dipole (d–d), dipole–quadrupole (d–q), and quadrupole–quadrupole (q–q) interactions, respectively. As illustrated in the inset of Fig. 6c, there can be approximated a linear relationship between x/I and I, that is, $\theta = 3$ ($\theta/3 = 1$), which is much less than 6. This indicates that non-radiative transition are not primarily mediated by the multi-polar interactions.[30,32] As referenced in our previous work, concentration quenching of Mn^{4+} in CZAO host is predominantly due to single-step energy transfer from Mn^{4+} ions to their adjacent quenching sites such as vacancy and interstitial defects.[30] In this study, by mitigating crystal defects such as Zn vacancies and oxygen vacancies through the synergistic introduction of B_2O_3 flux and B doping, the effective Mn^{4+} doping concentration is increased greatly. Concurrently, high QE is also achieved. As shown in Fig. 6d, phosphors with Mn^{4+} doping concentration ranging from 1% to 5% ($0.1 \leq x \leq 0.5$) exhibited high QE above 90%. For example, the QE values were approximately 93% for x = 0.1, 92% for x = 0.3, and 91% for x = 0.5. Notably, the sample with a high Mn^{4+} doping level of 5% (x = 0.5) exhibits intense absorption in the blue-to-NUV spectral region and high QE of over 90%, which is exceptional for Mn^{4+}-activated oxides and comparable to some superior fluorides such as K_2SiF_6:Mn^{4+}.

Fig. 7a and b show the temperature-dependent PLE and PL spectra of a representative sample, $Ca_{14}Zn_6Al_{9.65}B_{0.15}Mn_{0.1}Mg_{0.1}O_{35}$ − 0.42% B_2O_3. Several phenomena are observed. The first is the variation in the positions of the excited states with temperature. As depicted in Fig. 7c, upon increasing the temperature from 80 K to 660 K, the ZPL emission energy, $E(^2E_g)_{ZPL}$, decreased slightly from 14 409 cm^{-1} to 14 332 cm^{-1}, a reduction of only 77 cm^{-1}. In contrast, the zero-phonon energy of the $^4T_{2g}$ level ($E(^4T_{2g})_{ZPL}$, determined by the Franck–Condon analysis of the PLE spectra) decreased significantly by 3376 cm^{-1}, from 19 531 cm^{-1} to 16 155 cm^{-1}. The strong temperature dependence of the $E(^4T_{2g})_{ZPL}$ can be attributed to two primary factors: (1) temperature-induced band broadening. As shown in Fig. 7d, for the $^4A_{2g} \rightarrow {}^4T_{2g}$ transition, the FWHM increased from ~2680 cm^{-1} at 80 K to ~4760 cm^{-1} at 660 K. The broadening was slow at cryogenic temperatures but became rapid as the temperature exceeded 270 K. This is because the optical absorption transition initiates from the lowest vibrational level of the ground state at cryogenic temperatures close to 0 K, and higher vibrational levels become involved as temperature increases, resulting in band broadening.[22] However, it should be noted that thermal broadening does not cause a shift in the ZPL energy due to temperature changes. Therefore, when fitting the PLE

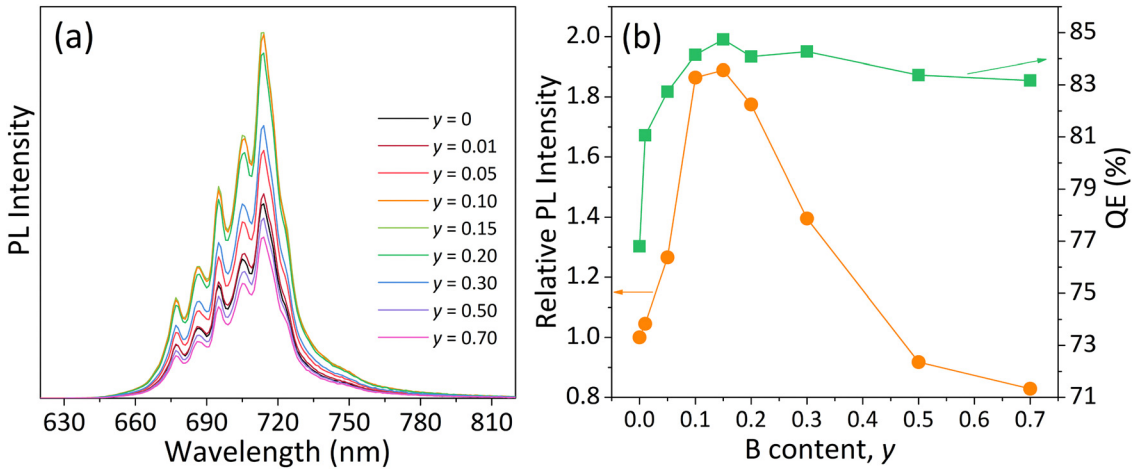

Fig. 5 (a) Room-temperature PL spectra of the $Ca_{14}Zn_6Al_{9.8-y}B_yMn_{0.1}Mg_{0.1}O_{35}$ phosphors. (b) Dependence of the PL intensity and QE on the B-doping concentration.

spectra at elevated temperatures, the obtained values of $E(^4T_{2g})_{ZPL}$ will be lower than the actual values due to the involvement of higher vibrational levels of the ground state (as well as $E(^4T_{1g,a})_{ZPL}$). (2) Downshift of the $^4T_{2g}$ energy level due to

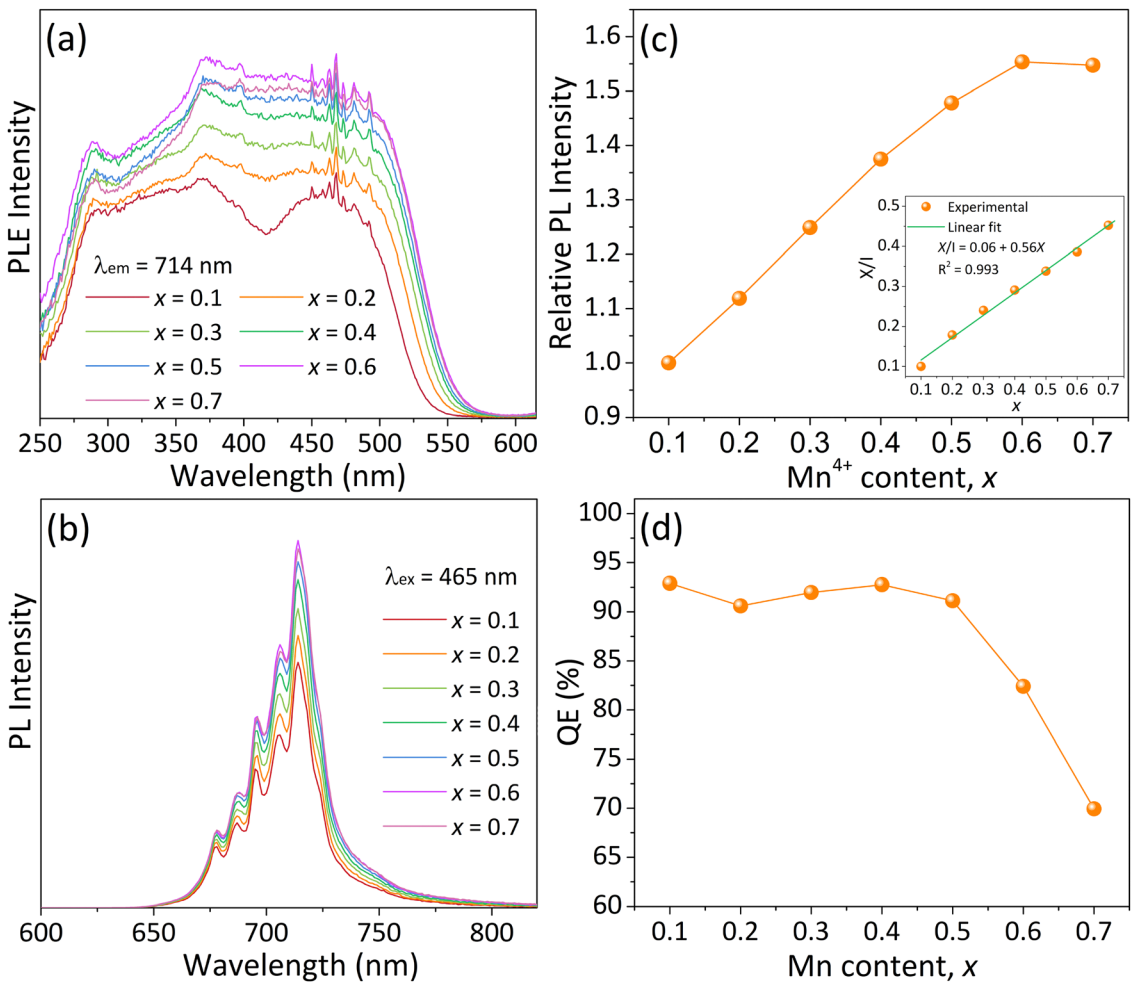

Fig. 6 (a) PLE (λ_{em} = 714 nm) and (b) PL (λ_{ex} = 465 nm) spectra of $Ca_{14}Zn_6Al_{9.85-2x}B_{0.15}Mn_xMg_xO_{35}$ – 0.42% B_2O_3 phosphors sintered at 1240 °C for 4 h. Dependence of the integrated PL intensity (c) and QE (d) on the Mn-doping concentration (x) of the $Ca_{14}Zn_6Al_{9.85-2x}B_{0.15}Mn_xMg_xO_{35}$ – 0.42% B_2O_3 phosphors.

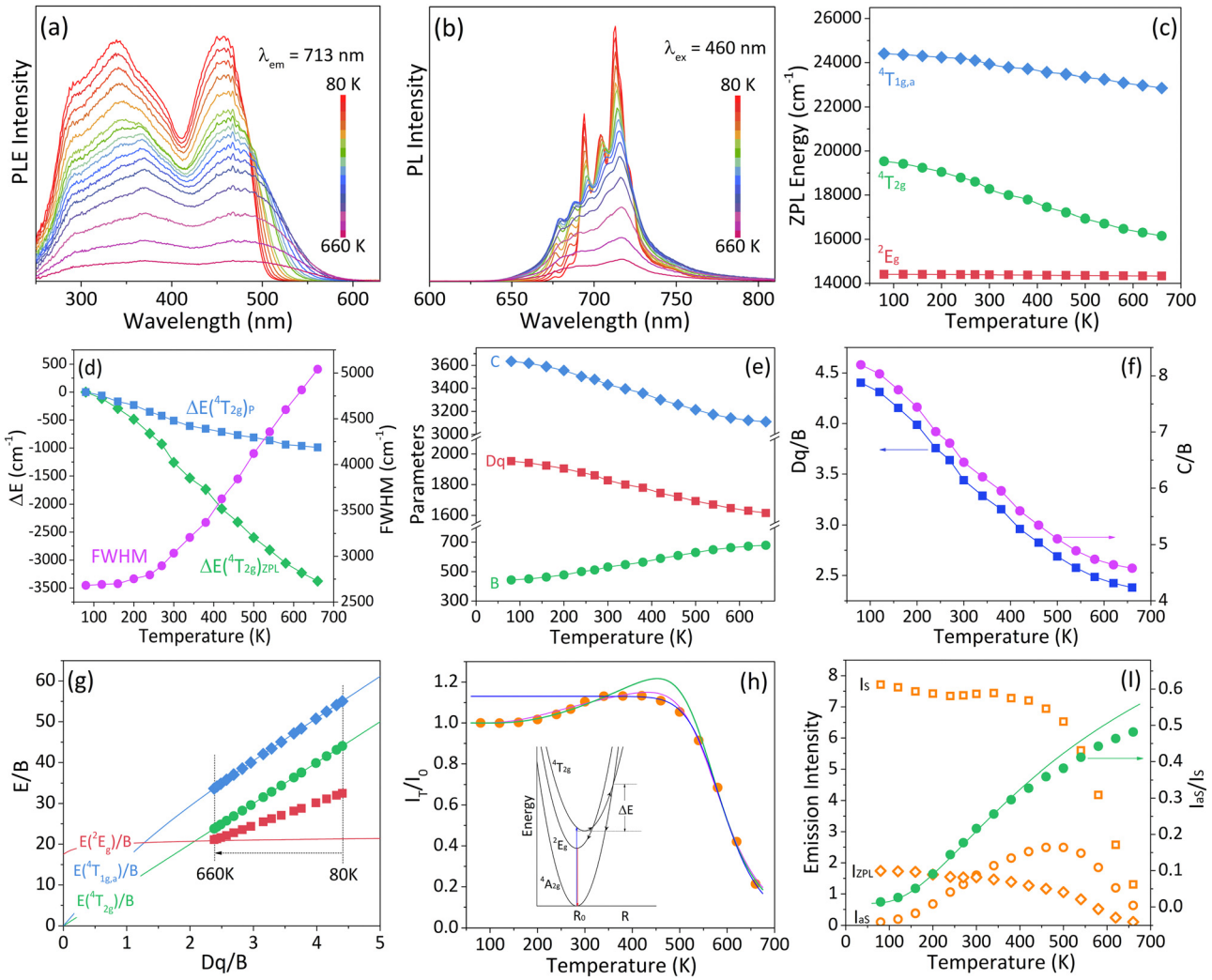

Fig. 7 Temperature-dependent photoluminescence properties of $Ca_{14}Zn_6Al_{9.65}B_{0.15}Mn_{0.1}Mg_{0.1}O_{35}$ – 0.42% B_2O_3. (a) PLE spectra, (b) PL spectra, (c) ZPL energies of the ^2E_g, $^4T_{2g}$, and $^4T_{1g,a}$ levels; (d) variation of the FWHM, the ZPL and peak energies ($\Delta E(^4T_{2g})_{ZPL}$ and $\Delta E(^4T_{2g})_P$, with respect to that at 80 K) of the $^4A_{2g} \rightarrow {}^4T_{2g}$ transition; (e) crystal-field and Racah parameters; (f) Dq/B and C/B; (g) excitation/emission energies (divided by B) *vs.* Dq/B on the Tanabe–Sugano energy diagram; (h) integrated PL intensity; (i) integrated PL intensities for the Stokes (I_S), anti-Stokes (I_{aS}), ZPL (I_{ZPL}) emission components, and the ratio of I_{aS} to I_S (I_{aS}/I_S). In (h), the inset is a configuration coordinate diagram schematically showing the thermal quenching of Mn^{4+}-activated phosphors; the blue solid line represents the fitted results using eqn (11), while the violet and green solid lines represent the fitted results using eqn (12) with $h\nu$ = 0.0653 and 0.0472 eV, respectively. The solid line in (i) represents the fitted result using eqn (10) with E_{ZPL} = 1.783 eV and $h\nu$ = 0.0472 eV.

thermal expansion of the host material. According to the point charge crystal field model, the ZPL energy of the $^4T_{2g}$ level, *i.e.*, the crystal-field splitting energy $10Dq$, is inversely proportional to a^5 (where a is the lattice constant).[36–38] Therefore, even a slight thermal expansion of the host lattice may lead to a significant change in $E(^4T_{2g})_{ZPL}$.[38] The effect of lattice dilation on the $^4T_{2g}$ energy position can be expressed as $E(T) = E(0) - 5E(0)\Delta l/l_0$ when Δl is far smaller than l_0 (where $\Delta l/l_0$ is the thermal lattice dilation, $E(T)$ and $E(0)$ are the energies of the $^4T_{2g}$ level at an elevated temperature T and the initial low temperature, respectively).[36] As shown in Fig. 7d, when the temperature was raised from 80 K to 660 K, the value of $E(^4T_{2g})_{ZPL}$ obtained from spectral analysis decreased by 3376 cm^{-1}, while the corresponding peak energy, $E(^4T_{2g})_P$, decreased by about 964 cm^{-1}. Assuming that the reduction in peak energy is primarily attributed to lattice expansion, the thermal expansion coefficient was calculated to be 1.7 × 10^{-5} K^{-1}, which is close to the experimentally determined value of 1.2 × 10^{-5} K^{-1} for CZAO.[39] Therefore, considering that the redshift of the ZPL energy is due to lattice thermal expansion rather than spectral thermal broadening, we can roughly estimate the change in $E(^4T_{2g})_{ZPL}$ based on the redshift of the peak position of the $^4T_{2g}$ transition band, instead of its low-energy tail. This method allows us to correct the $E(^4T_{2g})_{ZPL}$ values at different temperatures, as illustrated in Fig. S1 (ESI†).

By utilizing the values of $E(^4T_{2g})_{ZPL}$, $E(^4T_{1g,a})_{ZPL}$, and $E(^2E_g)_{ZPL}$ determined from the PLE and PL spectra, the crystal-field and Racah parameters Dq, B, and C can be calculated using the following equations:[30,40]

$$Dq = E(^4T_{2g})_{ZPL}/10 \quad (3)$$

$$B = \frac{(\Delta E_T/Dq)^2 - 10(\Delta E_T/Dq)}{15(\Delta E_T/Dq - 8)}Dq \quad (4)$$

$$C = \frac{E(^2E_g)_{ZPL} - 7.9B + 1.8B^2/Dq}{3.05} \quad (5)$$

where

$$\Delta E_T = E(^4T_{1g,a})_{ZPL} - E(^4T_{2g})_{ZPL} \quad (6)$$

It should be noted that eqn (5) is an approximate relationship obtained by diagonalizing the matrix elements of the crystal field and Coulomb interaction for the ^2E excited states of Cr^{3+} ions, and it is valid within the range of values where $1.5 < Dq/B < 3.5$ and $3 < C/B < 5$, as proposed by Henderson and Imbusch.[40] Recently, Brik *et al.* introduced an alternative equation:[41]

$$C = \frac{E(^2E_g)_{ZPL} - 8.0429B + 1.9915B^2/Dq}{3.0377} \quad (7)$$

which is valid within the parameter ranges of $1.6 < Dq/B < 4.9$ and $2.4 < C/B < 9.2$. In this study, the values of C under different temperatures were calculated using both formulas (5) and (7), with the results presented in Fig. S2 (ESI†). Evidently, there was a negligible discrepancy between the C values derived from the two equations, with an error margin of less than 0.1%. It was found that with the increase in temperature, both Dq and C decreased, while B increased, as shown in Fig. 7e. Consequently, with increasing temperature from 80 K to 660 K, the ratio Dq/B diminished from 4.40 to 2.38, and C/B decreased from 8.20 to 4.58, as shown in Fig. 7f. These observations demonstrate the validity of eqn (5) within the ranges of $2.38 < Dq/B < 4.40$ and $4.58 < C/B < 8.20$ in the context of this study. From a mathematical perspective, the equivalence between eqn (5) and (7) can be readily proven. When $2.1 \leq Dq/B \leq 5$ and $3 < C/B < 10$, the divergence in the values of $E(^2E_g)_{ZPL}$ calculated using eqn (5) and (7) is less than 85 cm^{-1}. This difference is considered negligible when compared to the typical value range of $E(^2E_g)_{ZPL}$ for Mn^{4+}-activated phosphors, which spans approximately from 13 800 to 16 200 cm^{-1}.

Fig. 7g presents the Tanabe–Sugano energy-level diagram for the experimentally determined ZPL energies of $^4T_{1g,a}$, $^4T_{2g}$, and ^2E_g levels at various temperatures. It was found that the ratios Dq/B, $E(^4T_{1g,a})_{ZPL}/B$, $E(^4T_{2g})_{ZPL}/B$, and $E(^2E_g)_{ZPL}/B$ decreased consistently with increasing temperatures. The values of $E(^4T_{1g,a})_{ZPL}/B$ changed almost linearly with Dq/B, which was in good accordance with the Tanabe–Sugano diagram. In contrast, the trend of $E(^2E_g)_{ZPL}/B$ with respect to Dq/B departed from the theoretical prediction, possibly due to the deviation of C/B ratio from the set value of 4.5. As is known, the Tanabe–Sugano diagram for d^3 configuration is constructed based on the assumptions that $B = 918$ cm^{-1} and $C/B = 4.5$.[42] Upon juxtaposing Fig. 7g and f, it became evident that at 660 K, with the C/B ratio at 4.58, the experimentally determined value of $E(^2E_g)_{ZPL}/B$ was in close alignment with the theoretical expectation. However, as the temperature decreased, the C/B ratio increased, diverging from the set value of 4.5. Concomitantly, the experimental values of $E(^2E_g)_{ZPL}/B$ deviated progressively from the predicted curve. Similarly, for the corrected $E(^4T_{2g})_{ZPL}$ and $E(^4T_{1g,a})_{ZPL}$ values based on the peak position of the corresponding transition bands, the obtained C/B ratio was around 8.25, and consequently, the $E(^2E_g)_{ZPL}/B$ values deviated significantly from the predicted curve, as shown in Fig. S1 (ESI†). However, it is important to note that the accurate determination of $E(^4T_{1g,a})_{ZPL}$ from the PLE spectra of Mn^{4+}-activated oxides (such as Fig. 6a) is nearly impossible. Moreover, even minor variations in the $E(^4T_{1g,a})_{ZPL}$ value can lead to considerable changes in the Racah parameters. Consequently, the calculated Racah parameters and their ratio C/B may deviate substantially from their actual values. To address this issue, Adachi proposed a new analytical model that sets the C/B ratio at a constant value of 4.7.[34] This approach allows for the calculation of $E(^4T_{1g,a})_{ZPL}$ and Racah parameters based on the easily and accurately determined values of $E(^2E_g)_{ZPL}$ and $E(^4T_{2g})_{ZPL}$.[34] Based on the correction of the $E(^4T_{1g,a})_{ZPL}$ value according to the change in the peak positon of the $^4T_{2g}$ transition band, we adopted this new model to fit the values of $E(^4T_{1g,a})_{ZPL}$ and Racah parameters. The results were shown in Fig. S1(e)–(h) (ESI†). As the temperature increased, $E(^4T_{2g})_{ZPL}$, $E(^4T_{1g,a})_{ZPL}$, and Dq/B only exhibited a slight decrease, while B and C remained virtually unchanged. Since the C/B ratio was set at 4.7—very close to 4.5—the calculated $E(^2E_g)_{ZPL}/B$ value aligned well with the predicted curve in the Tanabe–Sugano diagram.

Another concern is the thermal quenching of the Mn^{4+} emission, particularly its anomalous behavior below room temperature. Fig. 7h shows the integrated emission intensity (I_{PL}) as a function of temperature. When the sample was heated steadily from an initial cryogenic temperature of 80 K, the I_{PL} increased gradually and reached a maximum at 420 K. Within the temperature range of 300–460 K, the I_{PL} remained relatively constant, varying between 110% and 113% of the initial intensity at 80 K. Above 500 K, however, the I_{PL} underwent a sharp decline due to the rapid increase of non-radiative transitions with temperature. The quenching temperature, $T_{0.5}$, defined as the temperature at which the I_{PL} drops to half of its initial value at a low temperature (80 K in this study), was determined to be approximately 600 K. Such a high quenching temperature is rarely achieved in Mn^{4+}-activated phosphors, and is fully compliant with the thermal stability requirements for luminescence in LEDs and laser diodes (LDs).

The anomalous increase in emission intensity as the sample temperature rises from cryogenic to elevated levels, has also been observed in other Mn^{4+}-activated phosphors, such as the classic A_2XF_6:Mn^{4+} (where A represents alkali metal ions such as K^+ and Na^+; X represents tetravalent cations such as Ti^{4+} and Si^{4+}).[43] This phenomenon is commonly referred to as ''negative thermal quenching''.[44] The account for its origination is customarily predicated on the recognition that the $^2E_g \rightarrow {}^4A_{2g}$ transition is spin- and parity-forbidden and gain intensity mainly through coupling with local lattice vibrations.[44,45] As shown in Fig. 7i, the ZPL emission intensity (I_{ZPL}) constituted less than 20% of the total emission and continued to decrease

with increasing temperature. In contrast, the anti-Stokes emission intensity (I_{aS}), which was very weak at 80 K, increased significantly with temperature up to 500 K. Therefore, the negative thermal quenching behavior of the phosphor between 80–420 K can be attributed mainly to the enhancement of anti-Stokes vibrations.[18,33] The Stokes and anti-Stokes radiative transition probabilities of vibronic emissions are determined by the thermal population of phonon modes, and their intensity can be described by[3,46]

$$I_S(T) = A(E_{ZPL} - h\nu)^4 \frac{\exp\left(\frac{h\nu}{k_B T}\right)}{\exp\left(\frac{h\nu}{k_B T}\right) - 1} \quad (8)$$

$$I_{aS}(T) = A(E_{ZPL} + h\nu)^4 \frac{1}{\exp\left(\frac{h\nu}{k_B T}\right) - 1} \quad (9)$$

$$\frac{I_{aS}(T)}{I_S(T)} = \left(\frac{E_{ZPL} + h\nu}{E_{ZPL} - h\nu}\right)^4 \exp\left(-\frac{h\nu}{k_B T}\right) \quad (10)$$

where A is a constant, k_B the Boltzmann constant, h the Planck constant, ν the average lattice vibration frequency; E_{ZPL} is the ZPL emission energy, and $I_S(T)$ and $I_{aS}(T)$ correspond to the Stokes and anti-Stokes emission intensity at temperature T, respectively. Eqn (8) and (9) indicate that both $I_{aS}(T)$ and $I_S(T)$ increase with temperature, and the difference is that $I_{aS}(T)$ rises rapidly from 0 (at 0 K) with temperature, while $I_S(T)$ shows only a mild variation and can be considered approximately constant at low temperature, as confirmed by the experimental data in Fig. 7i. Consequently, their ratio, $I_{aS}(T)/I_S(T)$, exhibits strong temperature dependence, as described by eqn (10). We fitted the experimental data using eqn (10), with the values of E_{ZPL} and $h\nu$ derived from emission spectra. The experimental results in Fig. 7b suggests that the emission energies of ZPL and vibrational modes depend slightly on temperature and can be considered temperature-independent constants. They were determined as E_{ZPL} = 14 386 cm^{-1} (1.783 eV), $h\nu_3$ = 559 cm^{-1}, $h\nu_4$ = 379 cm^{-1}, $h\nu_6$ = 206 cm^{-1}. The average lattice vibration energy was calculated as $h\nu$ = 381 cm^{-1} (0.0472 eV), and the value of $((E_{ZPL} + h\nu)/(E_{ZPL} - h\nu))^4$ was 1.235. Consequently, eqn (10) can be written as $I_{aS}(T)/I_S(T) = 1.235\exp(-0.0472/(k_B T))$, with the calculated results shown as the green solid line in Fig. 7i. Obviously, the experimental data for $I_{aS}(T)/I_S(T)$ agreed well with the fitted curve within the range of 80–400 K. Beyond 400 K, the experimental data deviated from the fitted curve, which was due to the aggravation of non-radiative transition at high temperature. In general, the thermal quenching can be described by the Arrhenius equation:[30]

$$I_T = \frac{I_0}{1 + D\exp\left(-\frac{\Delta E}{k_B T}\right)} \quad (11)$$

where I_0 is the initial emission intensity at the starting temperature (ideally, 0 K), I_T is the emission intensity at an elevated temperature T, D is a rate constant for the thermal quenching process, and ΔE is the thermal quenching (or activation) energy. Taking the vibronic emissions (expressed by eqn (8) and (9)) and the normal thermal quenching (expressed by eqn (11)) into consideration simultaneously, the temperature dependence of the PL intensity is proposed to be[21,30]

$$I_T = \frac{I_0 \coth\left(\frac{h\nu}{2k_B T}\right)}{1 + D_1\exp\left(-\frac{\Delta E_1}{k_B T}\right) + D_2\exp\left(-\frac{\Delta E_2}{k_B T}\right)} \quad (12)$$

where D_1 and D_2 are constants, ΔE_1 and ΔE_2 are quenching energies *via* different pathways.[44,45] The larger ΔE_1 represents the thermal quenching energy. For Mn^{4+} ions, the luminescence quenching can be assigned to the thermally activated crossover *via* the $^4T_{2g}$ excited state since the parabolas of ^2E_g and $^4A_{2g}$ states in the configurational coordinate (CC) diagram are parallel (ΔR = 0) and do not cross (see Fig. 7h).[24] Therefore, the value of ΔE_1 is the energy difference between the lowest $^4T_{2g}$ state and the $^4T_{2g}$–$^4A_{2g}$ crossing point in the CC model (note that some literature also attributes it to the energy difference between the lowest ^2E_g state and the $^4T_{2g}$–$^4A_{2g}$ crossing point[24,47]), and D_1 is the rate constant for this thermal quenching process.[24] The introduction of the smaller ΔE_2 is based on the consideration of crystal defects, which act as non-radiative recombination centers, and the value of D_2 reflects the concentration of these defects.[44,45]

In general, eqn (11) works well for most phosphors, but it often fails with those activated by Mn^{4+} ions. As shown in Fig. 7h, eqn (11) can describe the thermal quenching behavior of $Ca_{14}Zn_6Al_{9.65}B_{0.15}Mn_{0.1}Mg_{0.1}O_{35}$ − 0.42% B_2O_3 at temperatures above 340 K appropriately, but it is ineffective at explain the temperature dependence of emission intensity below room temperature. On the contrary, eqn (12) can describe the temperature dependence of luminescence intensity in Mn^{4+}-activated phosphors adequately with parameters $h\nu$ = 0.0653 eV, D_1 = 1 100 000, ΔE_1 = 0.685 eV, D_2 = 2.850, and ΔE_2 = 0.095 eV, as indicated by the violet solid line in Fig. 7h. It should be noted that the fitting value of $h\nu$ deviates from the average lattice vibration energy (0.0472 eV). On the other hand, when setting $h\nu$ to 0.0472 eV, the fitting curve of eqn (12) aligned well with the experimental data at temperatures below 340 K and above 540 K, with fitted values of ΔE_1 and ΔE_2 being 0.685 eV and 0.0443 eV, respectively. However, there was a palpable deviation in the 340–540 K range. Based on the above observation, we propose that the origin of this discrepancy lies in the fact that eqn (12) captures the relationship between vibronic emissions and temperature but neglects the effect of ZPL emission, which decreases with increasing temperature as described by eqn (11). Therefore, eqn (12) is suitable for Mn^{4+}-activated phosphors with weak ZPL emission, such as K_2SiF_6:Mn^{4+}, $BaSiF_6$:Mn^{4+}, Cs_2NbOF_5:Mn^{4+}, and Ba_2LaTaO_6:Mn^{4+}. Yet, it falls short for phosphors with strong ZPL emission, like Rb_2GeF_6:Mn^{4+}, $Na_5Zr_2F_{13}$:Mn^{4+} and $Ca_{14}Zn_6Al_{10}O_{35}$:Mn^{4+}. Adachi integrated the temperature characteristics of ZPL, Stokes, and anti-Stokes emissions, and took the contribution of acoustic phonon modes into consideration, constructing a complex thermal quenching model (for details, see review articles[44,48]).

However, it should be kept in mind that, the emission spectrum of Mn^{4+} ions is greatly influenced by the crystal structure, composition, and crystalline quality of the host, and the contributions of optical and acoustic phonons vary significantly across different materials. Furthermore, the impact of lattice thermal expansion on metal–ligand distance and the resulting changes in crystal-field strength should not be overlooked. Therefore, developing a thermal quenching model that is physically meaningful and universally applicable for Mn^{4+}-activated phosphors remains a significant challenge.

Fig. 8a presents the PL decay curves of $Ca_{14}Zn_6Al_{9.65}B_{0.15}Mn_{0.1}Mg_{0.1}O_{35}$ − 0.42% B_2O_3 measured between 80 and 630 K. At temperature below 530 K, the decay curves exhibited mono-exponential behavior, which suggests that radiative transition is predominant and thus highlights the excellent thermal stability of the phosphor. At higher temperatures of 580 K and 630 K, the bi-exponential fitting was more in line with the experimental data, indicating that the non-radiative transition becomes significant. Fig. 8b shows the temperature dependence of decay lifetime (τ), which decreased from 6.002 ms at 80 K to 0.969 ms at 630 K. In most phosphors, the decrease in decay lifetime τ and emission intensity I_{PL} with temperature is mainly due to the enhancement of non-radiative transitions. Consequently, the lifetime typically exhibits a temperature dependence that mirrors the emission intensity, which can be described by the Arrhenius equation:[38,45]

$$\tau(T) = \frac{\tau_0}{1 + A\exp\left(-\frac{\Delta E}{k_B T}\right)} \quad (13)$$

or alternatively,

$$\tau(T) = \frac{\tau_R}{1 + \left(\frac{\tau_R}{\tau_{NR}}\right)\exp\left(-\frac{\Delta E}{k_B T}\right)} \quad (14)$$

where A is a constant, ΔE is the thermal activation energy, τ_0 and $\tau(T)$ are the lifetimes at the initial temperature (ideally, T = 0 K) and higher temperature T, while τ_R and τ_{NR} are radiative and non-radiative lifetimes, respectively. Eqn (15) and (16) are actually equivalent if we set $\tau_0 = \tau_R$ and $A = \tau_R/\tau_{NR}$.

However, for Mn^{4+}-activated phosphors, the decay lifetime often displays a temperature dependence that diverges significantly from the behavior of luminescence intensity. Particularly at low temperatures, the I_{PL} tends to increase to some extent with temperature, while the lifetime τ decreases consistently. This phenomenon was also observed in the CZAO:Mn^{4+} phosphors in this study. As the temperature increased from 80 K to 300 K, the I_{PL} increased by about 10% (Fig. 7i), while τ decreased by approximately one-third (Fig. 8b). Obviously, this significant decrease in τ is not due to thermal quenching, as the QE at room temperature is higher than 90% (Fig. 6d). Consequently, the variation of τ with temperature does not follow eqn (13), as indicated by the curve (iii) in Fig. 8b.

To explain the diminishing lifetime of Mn^{4+} luminescence with temperature, it is essential to understand the luminescence mechanism of Mn^{4+} in solid hosts. As we know, the $^2E_g \rightarrow {}^4A_{2g}$ transition is originally forbidden due to spin and parity selection rules. However, the spin–orbit coupling mixes the ^2E_g and $^4T_{2g}$ states, relaxing the spin selection rules and allowing the observation of the ZPL emission.[44] Additionally, the asymmetric distortion of the [MnO_6] octahedral, caused by the interaction between electrons and lattice vibrations, makes this transition partially parity-allowed.[45] This relaxation is achieved through coupling with the odd-symmetry vibrations of the [MnO_6] octahedron (ν_3, ν_4, and ν_6 modes), which results in the emission spectrum typically containing strong Stokes and anti-Stokes peaks ($h\nu_3$, $h\nu_4$, and $h\nu_6$).[44] The weakening of selection rules leads to an increase in transition probability and a decrease in lifetime τ. At low temperatures where thermal quenching has not yet begun, the Stokes and anti-Stokes radiative transition probabilities of vibronic emissions increase with rising temperature. According to eqn (8) and (9), the intensity of vibronic emissions can be expressed as $I(T) = I_S(T) + I_{aS}(T) = I_0\coth(h\nu/(2k_BT))$, which is essentially the numerator term of the luminescence thermal quenching eqn (12). Correspondingly, the variation of τ with temperature can be

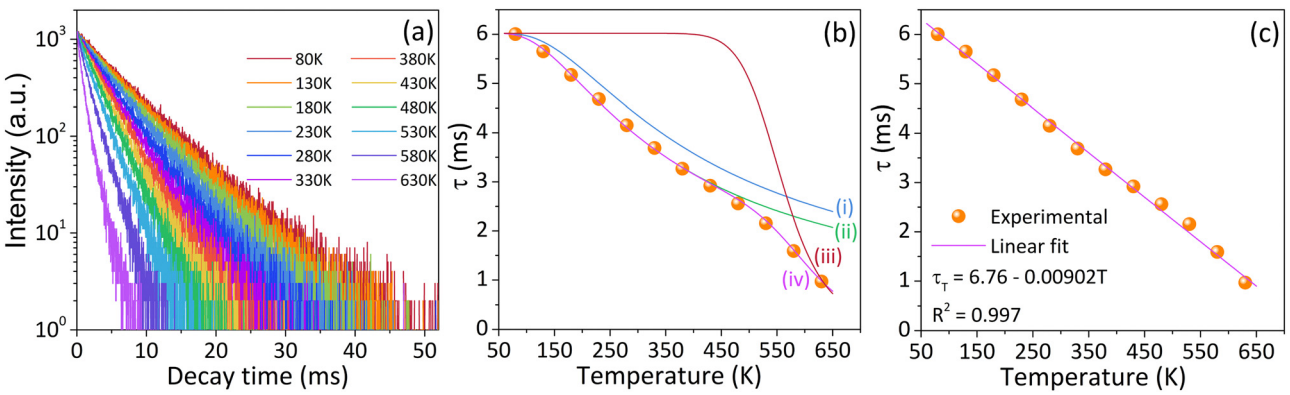

Fig. 8 (a) PL decay curves at 80–630 K for $Ca_{14}Zn_6Al_{9.65}B_{0.15}Mn_{0.1}Mg_{0.1}O_{35}$ − 0.42% B_2O_3. (b) and (c) Temperature dependence of the decay lifetime. The solid lines in (b) represent fits to eqn (15) with $h\nu$ = 0.0472 eV (curve (i)) or $h\nu$ = 0.0402 eV (curve (ii)), eqn (13) with ΔE = 0.685 eV (curve (iii)), and eqn (16) with $h\nu$ = 0.0402 eV and ΔE = 0.685 eV (curve (iv)), respectively. The solid line in (c) gives the linear fit.

expressed as:[24]

$$\tau_R(T) = \frac{\tau_0}{\coth\left(\frac{h\nu}{2k_BT}\right)} \quad (15)$$

where $\tau_R(T)$ is the radiative lifetime at temperature T. As indicated by curve (ii) in Fig. 8b, when the temperature is below 430 K, the fitting curve of eqn (15) with $h\nu$ = 0.0402 eV matches the experimental data well. However, it is noted that this fitted energy does not correspond to any vibrational mode of the [MnO_6] complex in CZAO:Mn^{4+},[30] and is lower than the aforementioned average vibrational energy (0.0472 eV). In contrast, the fitting result using $h\nu$ = 0.0472 eV (curve (i) in Fig. 8b) exhibited a slower decay rate than the experimental observation. The reason is that eqn (15) only takes into account the effect of lattice vibrations, neglecting the spin–orbit coupling between the ^2E_g and $^4T_{2g}$ states.[44] As shown in Fig. 7d, as the temperature increased, the energy separation between the ^2E_g and $^4T_{2g}$ states decreased significantly, which promoted the mixing of these states, and thus further reduced the decay lifetime.

At temperature higher than 430 K, the fitting curve of eqn (15) deviated from the experimental data, indicating the onset of thermal quenching. Substituting eqn (15) into eqn (14), we can get:

$$\tau(T) = \frac{\tau_0}{\coth\left(\frac{h\nu}{2k_BT}\right) + \frac{\tau_0}{\tau_{NR}}\exp\left(-\frac{\Delta E}{k_BT}\right)} \quad (16)$$

As indicated by curve (iv) in Fig. 8b, eqn (16) with ΔE = 0.685 eV and $h\nu$ = 0.0402 eV can well describe the variation of decay lifetime with temperature.

3.4. Potential application of $Ca_{14}Zn_6Al_{9.85-2x}B_{0.15}Mn_xMg_xO_{35}$ – B_2O_3 phosphors

The principal application of red-emitting phosphors is in white LEDs to improve their color rendering performance. However, in the case of Mn^{4+}-activated oxides, including CZAO:Mn^{4+}, their emission spectra fall predominantly within the deep-red spectral region with wavelengths exceeding 650 nm, which is less perceptible to the human eye. As a result, they are not commonly used in white LEDs for general lighting, except in full-spectrum products that require an extremely high level of color rendering and gamut. Despite this, they have found significant applications in indoor agricultural LEDs. As illustrated in Fig. 9a, the EL spectrum of the LED device, which was composed of a blue LED chip and a representative CZAO:Mn^{4+} phosphor ($Ca_{14}Zn_6Al_{9.25}B_{0.15}Mn_{0.3}Mg_{0.3}O_{35}$ – 0.42% B_2O_3), showed strong deep-red emission between 680–730 nm. This emission aligned well with the absorption spectrum of P_{FR}, and overlapped with the absorption spectra of P_R and chlorophyll *a* and *b* to some extent, which indicates that B-modified CZAO:Mn^{4+} phosphor is highly beneficial for the growth of indoor plants.

Another potential application of B-modified CZAO:Mn^{4+} lies in ratio optical thermometers. As mentioned above, the dependence of its decay lifetime on temperature can be described by a complex exponential function, namely eqn (16) (see Fig. 8b). In fact, as shown in Fig. 8c, this relationship can be simplified to a linear function: $\tau(T)$ = 6.76 – 0.00902T, with a high R-square of 0.997. This characteristic renders CZAO:Mn^{4+} suitable for use in luminescent thermometers, as it allows for a constant absolute sensitivity of 0.00902 ms K^{-1}, a value that is large enough to be measured with high precision. As reported in the vast literature, most phosphor-based luminescent thermometers exhibit sensitivity that varies with temperature, which complicates practical operations and may result in significant

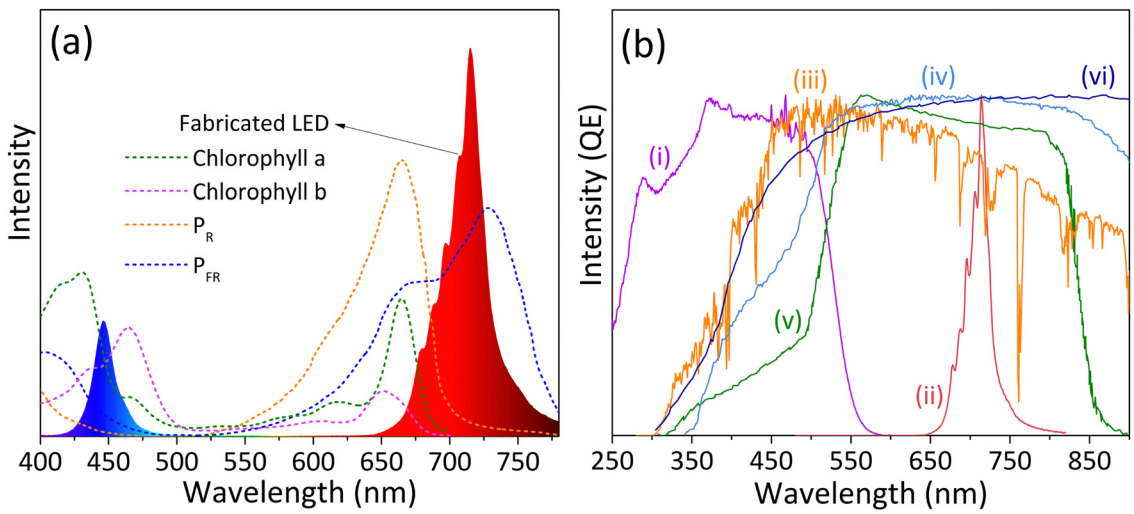

Fig. 9 (a) Comparison of the absorption spectra of chlorophyll *a* and *b*, phytochrome P_R and P_{FR} with the EL spectrum of LED device assembled by 450 nm blue LED chip and $Ca_{14}Zn_6Al_{9.25}B_{0.15}Mn_{0.3}Mg_{0.3}O_{35}$ – 0.42% B_2O_3 phosphor. (b) Modification of solar spectrum using Mn^{4+}-doped $Ca_{14}Zn_6Al_{10}O_{35}$ phosphor. (i) PLE and (ii) PL spectra of $Ca_{14}Zn_6Al_{8.85}B_{0.15}Mn_{0.5}Mg_{0.5}O_{35}$ – 0.42% B_2O_3 phosphor, (iii) AM1.5 solar spectrum, and typical wavelength-dependent QE curve of (iv) Cu(In,Ga)Se_2, (v) CdS-CdTe, and (vi) c-Si solar cells.

errors within certain temperature ranges. In contrast, for B-modified CZAO:Mn^{4+} phosphors, their linear variation of decay lifetime with temperature provides convenience for practical applications.

The B-modified CZAO:Mn^{4+} phosphor also holds significant potential in the spectral conversion of solar cells. The conversion of sunlight into electricity through photovoltaic devices is an appealing approach for generating green and renewable energy. However, typical semiconductor-based solar cells that have reached a certain level of maturity, such as crystalline silicon (c-Si), CdS-CdTe, and Cu(In,Ga)Se_2 (CIGS), fail to fully utilize the entire solar spectrum.[12,49–51] As shown in Fig. 9b, the QE of these solar cells drops sharply in the short-wavelength region below 520 nm. Meanwhile, the absorption in the long-wavelength region is also cut off due to their inherent material limitations. As a result, these solar cells can efficiently convert only 40% to 60% of the total solar radiation, with theoretical conversion efficiency limits around 30%.[52–54] This constraint impedes the cost competitiveness of solar energy relative to traditional fossil fuels.[55]

Considering that sunlight with wavelengths shorter than 520 nm accounts for about 20% of the total solar radiation, it is essential to absorb these high-energy photons using phosphors and converting them into low-energy photons within the high spectral response range of photovoltaic materials to improve the overall efficiency of solar cells. Historically, research on spectral converters has focused mainly on phosphors activated by rare earth ions such as Yb^{3+}, Nd^{3+}, and Dy^{3+}.[56] However, these phosphors exhibit only weak and narrow f–f excitation lines in the near-ultraviolet to visible light region due to the selection rules, which restricts their practical application.[56] In contrast, $Ca_{14}Zn_6Al_{9.25}B_{0.15}Mn_{0.3}Mg_{0.3}O_{35}$ − B_2O_3 phosphors can strongly absorb sunlight in the range of 250–520 nm and emit intense deep-red light within the 650–780 nm range (see Fig. 6 and 9b), where the absorption and conversion efficiencies of c-Si, CIGS and CdS-CdTe solar cells are at a high level. The QE of this down-conversion exceeds 90% (Fig. 6d), indicating that the spectral conversion strategy based on the CZAO:Mn^{4+} phosphors can improve the overall energy conversion efficiency of solar cells markedly. Besides, the temperature stability of the CZAO:Mn^{4+} phosphors is a notable advantage. Photovoltaic devices operate at temperature higher than ambient temperature, potentially exceeding 360 K in extreme cases. Therefore, phosphors used for solar spectrum modification must possess excellent thermal stability to avoid photoluminescence thermal quenching.[56] As mentioned previously, the quenching temperature $T_{0.5}$ of the B-modified CZAO:Mn^{4+} phosphors is as high as 600 K. More specifically, as the temperature rises from 270 K to 380 K, the light absorption capability decreases by only about 12%, while the emission intensity increases by 6%, which ensures effective modification of solar spectrum.

4. Conclusions

In summary, we synthesized B-modified $Ca_{14}Al_{10}Zn_6O_{35}$:Mn^{4+} phosphors through the conventional solid-state reaction method and investigated the effects of B_2O_3 flux and lattice B doping on their photoluminescence properties. It is found that B_2O_3 not only serves as a flux to reduce the sintering temperature, minimize Zn volatilization, and enhance the crystallinity of the phosphors, but also incorporates B^{3+} ions into the lattice sites of $Ca_{14}Al_{10}Zn_6O_{35}$, further refining the luminescence performance. Within the $Ca_{14}Zn_6Al_{9.8}Mn_{0.1}Mg_{0.1}O_{35}$ − z% B_2O_3 system, optimizing the B_2O_3 content to 0.42 wt% results in a remarkable enhancement, by 87% and 112% respectively, in light absorption and emission, with QE improving from 76.8% to 84.6%. For the $Ca_{14}Zn_6Al_{9.8-y}B_yMn_{0.1}Mg_{0.1}O_{35}$ samples, it is demonstrated that the solid solubility of B is approximately 2%, and the optimal doping concentration is 1.5% (y = 0.15), at which the phosphors exhibit the strongest light absorption and emission, along with the highest QE. These findings lead to the fabrication of $Ca_{14}Zn_6Al_{9.85-2x}B_{0.15}Mn_xMg_xO_{35}$ − 0.42% B_2O_3 phosphors. By virtue of the synergistic effects of B_2O_3 flux and lattice B doping, the optimal Mn^{4+} doping concentration is increased significantly from 1% to 6%, which greatly strengthens the absorption of NUV/blue light and enhances their potential for commercial applications. Notably, samples with Mn^{4+} doping concentrations between 1% and 5% show high QE exceeding 90%. Moreover, the phosphors exhibit a negative thermal quenching phenomenon between 80–420 K, with an extremely high thermal quenching temperature $T_{0.5}$ of about 600 K, outperforming most reported Mn^{4+}-activated phosphors. Such oxide phosphors, characterized by high Mn^{4+} doping concentration, high QE, and superior thermal stability, are rarely documented. The outstanding performance of these phosphors also suggests their broad application prospects in areas such as indoor agricultural lighting, optical thermometers, and solar cells. We hope that this study provides valuable insights for the development of Mn^{4+}-activated red phosphors.

Data availability

The data that support the findings of this study are available on request from the corresponding author.

Conflicts of interest

There are no conflicts of interest to declare.

Acknowledgements

This work was supported by the Science and Technology Project of Fujian Province (2023H0044) and Fujian Science & Technology Innovation Laboratory for Optoelectronic Information of China (No. 2021ZZ113).

References

1 M. Abraham, K. K. Thejas, A. K. Kunti, N. Amador-Mendez, R. Hernandez, J. Duras, K. G. Nishanth, S. K. Sahoo,

M. Tchernycheva and S. Das, *Adv. Opt. Mater.*, 2024, **12**, 2401356.
2 Y. B. Hua, J. S. Yu and L. Li, *J. Adv. Ceram.*, 2023, **12**, 954–971.
3 S. Adachi, *ECS J. Solid State Sci. Technol.*, 2020, **9**, 016001.
4 A. G. Bispo-Jr, L. F. Saraiva, S. A. M. Lima, A. M. Pires and M. R. Davolos, *J. Lumin.*, 2021, **237**, 118167.
5 G. Li, Y. Tian, Y. Zhao and J. Lin, *Chem. Soc. Rev.*, 2015, **44**, 8688–8713.
6 Y. Liu, Z. Li, W. Zhang, X. Yan, P. Guo and J. Yan, *Dalton Trans.*, 2024, **53**, 11800–11808.
7 R. Cao, X. Hu, J. Nie, B. Lan, J. Wang, T. Chen, Y. Chen and J. Wang, *J. Mol. Struct.*, 2024, **1318**, 139405.
8 Z. Wang, Y. Li, X. Yang, B. Wang, R. Mi and Y. Liu, *J. Mater. Chem. C*, 2024, **12**, 18840–18848.
9 M. Zhao, H. X. Liao, L. X. Ning, Q. Y. Zhang, Q. L. Liu and Z. G. Xia, *Adv. Mater.*, 2018, **30**, 1802489.
10 J. Gao, H. Zhu, R. Li, D. Huang, B. Luo, W. You, J. Ke, X. Yi, X. Shang, J. Xu, Z. Deng, L. Xu, W. Guo and X. Chen, *J. Mater. Chem. C*, 2019, **7**, 7906–7914.
11 P. K. Tawalare, *AIP Adv.*, 2021, **11**, 100701.
12 P. K. Tawalare, P. D. Belsare and S. V. Moharil, *J. Alloys Compd.*, 2020, **825**, 154007.
13 E. Klampaftis, D. Ross, K. R. McIntosh and B. S. Richards, *Sol. Energy Mater. Sol. Cells*, 2009, **93**, 1182–1194.
14 R. J. Xie, N. Hirosaki, T. Suehiro, F. F. Xu and M. Mitomo, *Chem. Mater.*, 2006, **18**, 5578–5583.
15 X. Q. Piao, K. Machida, T. Horikawa, H. Hanzawa, Y. Shimomura and N. Kijima, *Chem. Mater.*, 2007, **19**, 4592–4599.
16 L. Wang, R. J. Xie, T. Suehiro, T. Takeda and N. Hirosaki, *Chem. Rev.*, 2018, **118**, 1951–2009.
17 Z. Yang, G. Lu, T. Yang, X. Zhou, L. Li, Y. Zhou and Z. Wang, *J. Phys. Chem. C*, 2024, **128**, 13612–13619.
18 H. Zhu, C. C. Lin, W. Luo, S. Shu, Z. Liu, Y. Liu, J. Kong, E. Ma, Y. Cao, R. S. Liu and X. Chen, *Nat. Commun.*, 2014, **5**, 4312.
19 T. K. Kuttiat, M. Abraham, A. K. Kunti, N. Amador-Mendez, M. Tchernycheva and S. Das, *ACS Appl. Mater. Interfaces*, 2023, **15**, 7083–7101.
20 J. Huang, P. Jiang, Z. Cheng, R. Wang, R. Cong and T. Yang, *Inorg. Chem. Front.*, 2023, **10**, 2776–2787.
21 S. Adachi, *J. Lumin.*, 2018, **202**, 263–281.
22 G. Blasse, *Luminescent Materials*, Springer-Verlag, Berlin, 1994.
23 S. Wang, T. Seto, B. Liu, Y. Wang, C. Li, Z. Liu and H. Dong, *Adv. Sci.*, 2023, **10**, 2204418.
24 T. Senden, R. J. A. van Dijk-Moes and A. Meijerink, *Light:Sci. Appl.*, 2018, **7**, 8.
25 D. L. Dexter and J. H. Schulman, *J. Chem. Phys.*, 1954, **22**, 1063–1070.
26 D. L. Dexter, *J. Chem. Phys.*, 1953, **21**, 836–850.
27 K. Shan, B. Jing, J. Han, H. Fei, Y. Zhou, X. Xu and X. Zhang, *J. Lumin.*, 2024, **269**, 120528.
28 Z. Lu, A. Fu, F. Gao, X. Zhang and L. Zhou, *J. Lumin.*, 2018, **203**, 420–426.
29 J. Liang, B. Devakumar, L. Sun, S. Wang, Q. Sun, H. Guo and X. Huang, *J. Alloys Compd.*, 2019, **804**, 521–526.
30 T. Lv, J. Q. Huang, C. L. Yang, Y. Wang, Q. F. Huang, J. Chen and W. Guo, *J. Mater. Chem. C*, 2022, **10**, 9773–9785.
31 F. Garcia-Santamaria, J. E. Murphy, A. A. Setlur and S. P. Sista, *ECS J. Solid State Sci. Technol.*, 2017, **7**, R3030–R3033.
32 T. Deng, S. Zhang, R. Zhou, T. Yu, M. Wu, X. Zhang, K. Chen and Y. Zhou, *Dalton Trans.*, 2022, **51**, 608–617.
33 T. Lv, J. Q. Huang, Z. H. Deng, C. L. Yang and W. Guo, *J. Alloys Compd.*, 2021, **874**, 159863.
34 S. Adachi, *ECS J. Solid State Sci. Technol.*, 2020, **9**, 046004.
35 J. Liang, L. Sun, B. Devakumar, S. Wang, Q. Sun, H. Guo, B. Li and X. Huang, *RSC Adv.*, 2018, **8**, 27144–27151.
36 C. J. Donnelly, S. E. Healy, T. J. Glynn, G. F. Imbusch and G. P. Morgan, *J. Lumin.*, 1988, **42**, 119–125.
37 S. Sugano, Y. Tanabe and H. Kaminura, *Multiplets of transition-metal ions in crystals*, Academic Press, New York, 1970.
38 S. Yan, *ECS J. Solid State Sci. Technol.*, 2021, **10**, 086005.
39 V. Kahlenberg and H. Kruger, *Z. Kristallogr. – Cryst. Mater.*, 2022, **237**, 219–232.
40 B. Henderson and G. F. Imbusch, *Optical spectroscopy of inorganic solids*, Clarendon Press, Oxford, 1989.
41 C. G. Ma, Y. Wang, D. X. Liu, Z. Li, X. K. Hu, Y. Tian, M. G. Brik and A. M. Srivastava, *J. Lumin.*, 2018, **197**, 142–146.
42 Y. Tanabe and S. Sugano, *J. Phys. Soc. Jpn.*, 1954, **9**, 766–779.
43 S. Yan, *ECS J. Solid State Sci. Technol.*, 2020, **9**, 106004.
44 S. Adachi, *ECS J. Solid State Sci. Technol.*, 2022, **11**, 036001.
45 S. Adachi, *ECS J. Solid State Sci. Technol.*, 2021, **10**, 026002.
46 T. Takahashi and S. Adachi, *J. Electrochem. Soc.*, 2008, **155**, E183–E188.
47 M. S. Kurboniyon, A. M. Srivastava, B. Lou, D. D. Nematov, A. Burhonzoda, T. Yamamoto, C. G. Ma and M. G. Brik, *Inorg. Chem.*, 2024, **63**, 21212–21221.
48 S. Adachi, *ECS J. Solid State Sci. Technol.*, 2022, **11**, 066001.
49 S. Ito, H. Matsui, K. Okada, S. Kusano, T. Kitamura, Y. Wada and S. Yanagida, *Sol. Energy Mater. Sol. Cells*, 2004, **82**, 421–429.
50 A. Virtuani, E. Lotter and M. Powalla, *Sol. Energy Mater. Sol. Cells*, 2006, **90**, 2141–2149.
51 J. Liu, K. Wang, W. Zheng, W. Huang, C. H. Li and X. Z. You, *Prog. Photovoltaics Res. Appl.*, 2013, **21**, 668–675.
52 M. A. Green and S. P. Bremner, *Nat. Mater.*, 2016, **16**, 23–34.
53 D. Yu, T. Yu, H. Lin, S. Zhuang and D. Zhang, *Adv. Opt. Mater.*, 2022, **10**, 2200014.
54 J. Yang, J. Wang, K. Zhao, T. Izuishi, Y. Li, Q. Shen and X. Zhong, *J. Phys. Chem. C*, 2015, **119**, 28800–28808.
55 W. Li, T. Chen, W. Xia, X. Yang and S. Xiao, *J. Lumin.*, 2018, **194**, 547–550.
56 P. K. Tawalare, V. B. Bhatkar, S. K. Omanwar and S. V. Moharil, *J. Alloys Compd.*, 2019, **771**, 534–540.